Microstructural Characterization of Internal Welding Defects and Their Effect on the Tensile Behavior of FSW Joints of AA2198 Al-Cu-Li Alloy

THOMAS LE JOLU, THILO F. MORGENEYER, ANNE DENQUIN,
MOHAMED SENNOUR, ANNE LAURENT, JACQUES BESSON,
and ANNE-FRANÇOISE GOURGUES-LORENZON

Internal features and defects such as joint line remnant, kissing bond, and those induced by an initial gap between the two parent sheets were investigated in AA2198-T851 friction stir welded joints. They were compared with the parent material and to defect-free welds obtained using a seamless sheet. The cross-weld tensile strength was reduced by the defects by less than 6 pct. The fracture elongation was not significantly affected in view of experimental scatter. Fracture location, however, changed from the thermomechanically affected zone (retreating side) to the defect in the weld nugget for the welds bearing a kissing bond and for some of the gap welds. The kissing bond was shown by EBSD to be an intergranular feature; it fractured under a normal engineering stress close to 260 MPa during an *in situ* SEM tensile test. Synchrotron tomography after interrupted tensile testing confirmed opening of the kissing bond. For an initial gap of 23 pct of the sheet thickness, intergranular fracture of copper-enriched or oxide-bearing grain boundaries close to the nugget root was evidenced. The stress and strain state of cross-weld specimens loaded under uniaxial tension was assessed using a 3D finite element, multi-material model, determined on the basis of experimental data obtained on the same specimens using digital image correlation.

I. INTRODUCTION

AMONG processes that have been developed to substitute riveting in lightweight structures, friction stir welding (FSW) offers the advantages of avoiding hot cracking and limiting component distortion. Application of this process to aluminum alloys has been extensively reviewed recently.[1] For certain processing conditions, internal flaws may appear. Internal cavities and tunneling defects could be detected at least in certain cases using non-destructive evaluation methods.[2] They may impair the ductility of the welded joints, in particular for high values of the rotational speed.[3,4] In most of aluminum friction stir welds, a discontinuous, wavy surface within the nugget referred to as "joint line remnant" (JLR), "lazy S," "zigzag curve," or "zigzag line" may be found after welding.[5–10] Such a feature is connected to the weld root and may induce fracture after severe bending of the weld. In this case, it is referred to as "kissing bond" (KB), "weak bond," or "root flaw".[6,11–15] Both JLR and KB seem to originate from insufficient mixing of matter close to the initial butt surfaces,[5–7,13,16] but KB results more specifically from a lack of pin penetration during welding. From TEM studies of 1050-H24 and 5052 alloys,[3,17] the poorly mixed oxide film close to the weld root seems to be discontinuous for the JLR but continuous and intergranular for the KB. Plastic flow and recrystallisation in the nugget have been characterized as a function of welding parameters (see *e.g.*,[18–22]); however, information about stirring conditions very close to the bottom surface of FSW joints is still lacking. As a whole, only scarce data are available from open literature and still need to be completed by considering other alloys.

Another kind of feature may appear if there is some distance (a "gap") left between the two sheets to be butt welded. Metallographic observations of cross sections showed that leaving such a gap caused the presence of cavities, such defects can be remediated by increasing the heat input energy.[12,23] Little data are available about the consequences of such a gap on the mechanical properties of the welded joint, in the case where no cavity can be detected by non-destructive evaluation. In addition, detection of tiny internal features, which could appear for lower values of the gap, is still out of reach of

THOMAS LE JOLU, formerly Ph.D. Student with MINES ParisTech, Centre des Matériaux, UMR CNRS 7633, BP 87, 91003 Evry Cedex, France, is now Research Engineer with the CEA Saclay, DMN/SEMI/LCMI, 91191 Gif-Sur-Yvette Cedex, France. THILO F. MORGENEYER, Researcher, MOHAMED SENNOUR, Research Engineer, ANNE LAURENT, Technical Assistant, JACQUES BESSON, Researcher, Director, and ANNE-FRANÇOISE GOURGUES-LORENZON, Professor in Materials Science and Engineering, are with the MINES ParisTech, Centre des Matériaux, UMR CNRS 7633. Contact e-mail: anne-francoise.gourgues@mines-paristech.fr ANNE DENQUIN, Deputy Director, is with the Department of Metallic Materials and Structures, Onera, 29 Avenue de la Division Leclerc, BP 72, 92322 Châtillon Cedex, France.
Manuscript submitted September 6, 2013.
Article published online September 6, 2014

conventional or even advanced non-destructive evaluation methods.[2]

The purpose of the current study was to investigate the microstructural characteristics of JLR, KB, and gap-induced features and their consequences on the mechanical behavior of FSW joints of an Al-Cu-Li alloy used for aircraft applications. This paper reports on microstructural characterization of the considered features as well as the monotonic tensile behavior of welded joints with or without controlled internal flaws (JLR, KB, and gap-induced flaws), including a three-dimensional finite element simulation of plastic flow of the weld. Effects of these features on the fatigue lifetime and failure mechanisms have been quantitatively addressed in a separate study.[9,24]

II. EXPERIMENTAL DETAILS

A. Material and Welded Joints

A 3.1-mm-thick sheet of AA2198-T851 was used in this study. Its chemical composition is Al-3.20 Cu-0.98 Li-0.31 Ag-0.31 Mg-0.11 Zr-0.04 Fe-0.03 Si (wt pct), and the aging conditions were 428 K (155 °C) for 16 hours. Pancake-shaped grains (15 to 20 μm in thickness) were observed throughout the thickness, except at the skin of the sheet, which was composed of coarser pancake grains (100 μm in thickness) over a depth of 0.5 mm (Figure 1). In the following, RD denotes the rolling direction of the sheet, TD denotes its long transverse direction, and ND denotes its short transverse direction. In the (TD, ND) plane, the Vickers hardness under a 100-g load was 150 ± 5 HV$_{0.1}$, except at mid-thickness (137 ± 5 HV$_{0.1}$.)

FSW joints, with the welding direction parallel to RD, were realized from coupons of 500 mm in length (parallel to RD) and 150 mm in width (parallel to TD). Optimized welding parameters ensured the absence of external defects such as flashes and of internal defects such as tunnels or cavities resulting from abnormal stirring.[25–27] Except otherwise stated to be suppressed the welding machine was displacement controlled with a traveling speed of 480 mm min^{-1}, a rotational speed of 1200 rpm, an adjustable pin length threaded tool with 13 mm in shoulder diameter, and 4.2 mm in pin diameter. The first 100 mm (150 mm when necessary)
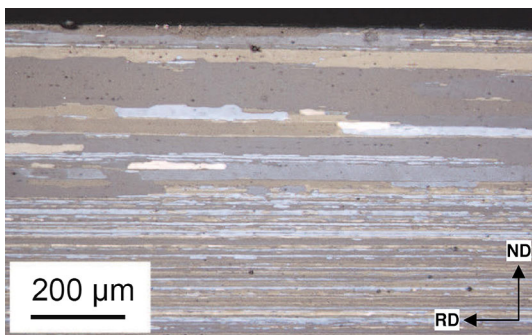

Fig. 1—Light optical micrograph of the base metal; coarser grains are revealed close to the surface.

of the weld was discarded from analysis to ensure that specimens were cut from a region where axial force (or axial displacement if load controlled) was stable (between 4 and 5 kN for the load-controlled conditions). Four kinds of welds were fabricated from the same sheet and investigated in the as-welded condition (Figure 2):

- "Sound" welds were made by moving the tool into a seamless sheet (*i.e.*, bead-on-plate welds). This ensures the absence of native oxide at blank edges just before welding;
- "JLR-bearing" welds resulting from welding two coupons with their natural oxide layer;
- "KB-bearing" welds as for JLR but with retracting the pin by 80 μm; this induces a distance of 200 μm between the bottom end of the pin and the bottom surface of the parent sheets, which changes stirring conditions within the weld;
- "Gap" welds were obtained with a constant clearance of either 0.3 mm ("Gap0.3": 10 pct of the parent sheet thickness) or 0.7 mm ("Gap0.7": 23 pct of the parent sheet thickness) between the coupons to be welded. These welds were realized under a constant load of 4 kN. The pin displacement was observed to stabilize after about 150 mm. The appearance of flashes at the upper side of these welds could not be totally avoided, but it did influence neither their microstructure nor their average mechanical behavior.

B. Microstructural Characterization

All welded joints were controlled for the presence of any KB-like feature. 10-mm-wide bands were cut perpendicularly to the weld and then bent using a hand vice, up to a bending angle of 90 deg, resulting in a bending radius of 7 mm. The weld root was at the apex of the bending specimen. Such severe bending induced crack initiation from the weld root of KB-bearing welds only. Cross-section samples were polished with diamond pastes and first etched by anodic oxidation (3 pct aqueous solution of tetrafluoroboric acid in water, under 30 V with respect to a pure aluminum electrode, for 2 to 3 minutes). Their microstructure was observed under polarized light optical microscopy (LOM). They were then further chemically etched with the Dix-Keller reagent (2 mL HF, 3 mL HCl, 20 mL HNO$_3$, and 175 mL distilled water). Further LOM observation under white light enabled to locate, if any, the JLR and KB features in the samples. To get more insight on the location of the KB with respect to the fine-grained microstructure close to the weld root, a cross section was prepared by polishing and etching with Ga$^+$ ions using a Jeol IB-09010CP cross-section polisher. A 50×125 μm^2 region was then analyzed using electron backscatter diffraction (EBSD) in a Leo 1450 VP scanning electron microscope (SEM). EBSD data were acquired using a TSL OIM® 5 system fitted to a Hikari fast camera. The operating parameters leading to satisfactory quality of EBSD patterns were as follows:
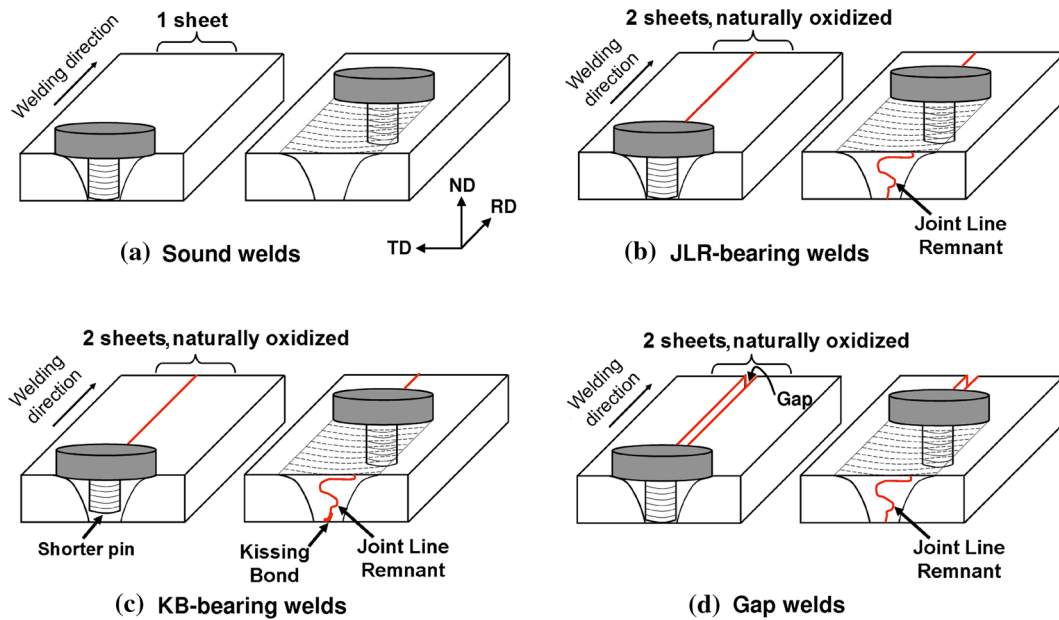
Fig. 2—Schematic drawing of (*a*) "sound" welds, (*b*) welds bearing a joint line remnant, (*c*) welds bearing a kissing bond, (*d*) welds with a gap left between the parent sheets.

a 70 deg tilt angle, a working distance of 22 mm, a high voltage of 30 kV, a probe current of 1 nA, and a hexagonal grid with a step size of 0.5 μm. In order to minimize introduction of artifacts, EBSD maps were processed without applying any data cleaning procedure. Backscattered electron images of the same region were also taken to investigate the presence of particles or films at the KB.

Particular regions of "Gap" welds, close to the weld root, were observed using transmission electron microscopy (TEM). Blanks for thin foils at (and parallel to) the bottom surface, parallel to the (RD, TD) plane, were extracted. They were slightly polished close to the weld root and then mechanically thinned from the upper surface of the weld, followed by Ar^+ ion milling using a Polishing Ion Precision System. Thin foils were observed using a Tecnai F20 microscope equipped with energy dispersive spectrometry (EDX), scanning transmission electron microscopy (STEM) together with high angle annular dark field (HAADF) imaging facilities.

C. *Mechanical Characterization*

Full-thickness smooth flat tensile specimens with a 64-mm-long and 12-mm-wide gauge part were cut across the welded joints, *i.e.*, along TD. They were tested at room temperature in laboratory air, using a 250-kN servohydraulic testing machine under displacement control. The initial elongation rate (averaged between two fiducial marks located at each side of the weld, over a distance of 14 mm) was 2.10^{-4} s^{-1}, with the weld at the center of the gauge region. Local strains were determined at one specimen edge thanks to a random black-and-white speckle deposited onto the specimen and to conventional strain field monitoring techniques. A 2048 $\times$ 2048 pixel^2 camera (one frame per second)

was used with a pixel size of 15 μm. Digital image correlation was carried out using Correli™ software[28,29] with 16 $\times$ 16 pixel^2 regions of interest (suited to the size of the zones to be characterized) and incremental calculation of displacements and strains.

The plastic anisotropy was characterized for the base metal using uniaxial tensile tests (same specimen geometry as above) along RD, TD, and the diagonal direction, DD, at 45 deg from RD in the RD–TD plane. Three tests were carried out per condition, except for "Gap" welds for which two tests were performed per condition. High reproducibility (within ~1 pct) of engineering stress–strain curves was found for a given testing condition.

To independently characterize the uniaxial tensile behavior of the weld nugget, full-thickness specimens (4 $\times$ 20 mm^2 in gauge) were cut from one sound weld and from one JLR-bearing weld, parallel to the welding direction. As a result, the gauge region only contained the weld nugget microstructure. For both base metal and weld nugget, Lankford coefficients, *r* (ratios of relative reduction in width to relative reduction in thickness), were calculated from the displacement of fiducial marks, under an isochoric deformation assumption.

Two full-thickness cross-weld specimens with edge notches in the middle of the nugget were also tested using a 100-kN servohydraulic testing machine. They had a total width of 18 mm, a notch radius of 0.5 mm, and a minimum width of 10 mm. Their geometry is illustrated together with the tensile curves in the following. A load line displacement rate of 10^{-3} mm s^{-1} was prescribed. The notch opening displacement was calculated by averaging measurements from clip extensometers attached to either notch of the specimen. These measurements were differed by less than 5 pct. Load *vs*

notch opening displacement curves agreed within less than 1 pct with each other for the two tests.

The conditions for KB opening were determined using uniaxial *in situ* tensile tests. Full-thickness smooth tensile specimens, with a gauge length of 13 mm and a gauge width of 3 mm, were pulled in tension inside the Leo 1450 VP SEM chamber equipped with a 5-kN tensile stage. A load line displacement rate of 3.3×10^{-3} mm s^{-1} was applied. The specimens were slightly polished, and the weld root was observed by locking the load line displacement several times during the test.

Fracture surfaces were observed using either the Leo 1450 VP SEM or a field emission gun Zeiss DSM 982 Gemini high resolution SEM, both under secondary electron imaging.

Following the results of *in situ* tensile tests, two $1 \times 1 \times 10$ mm^3 samples were cut from a KB-bearing weld after loading in uniaxial tension up to 380 MPa, followed by unloading. 3D images of samples were obtained from microtomography analysis at the European Synchrotron Radiation Facility (ID19 line, photon energy 19 keV, voxel size 0.7 μm, 1500 radiographs, one radiograph every 0.7 s).

III. EXPERIMENTAL RESULTS AND DISCUSSION

A. Microstructure of the Welded Joints

The grain structure of all welded joints was similar to that illustrated in Figure 3(a), showing a well-recrystallized nugget (120 HV$_{0.1}$) with equiaxed grains of 10 μm in average size. At either side of the nugget, two thermomechanically affected zones (TMAZs) showed heavily deformed grains and hardness close to 110 HV$_{0.1}$. The heat-affected zones (HAZs) exhibited the same grain morphology as the base metal and a

hardness gradient between the hardness of the TMAZ and that of the base metal (*i.e.*, ~137 to 150 HV$_{0.1}$). Such "W-shaped" hardness profiles are in agreement with the literature data[30–39] and quantitatively consistent with those found by Denquin *et al.*[40] in an as-welded 3-mm-thick AA2098-T8 FSW joint.

Both JLR and KB flaws appear as a thin line in metallographic cross sections (Figures 3(b) and (c)). The KB is inclined by about 20 deg from the sheet plane, over 20 to 30 μm close to the weld root. It turns to be perpendicular to the rolling plane underneath, over a distance of 100 to 130 μm. In agreement with the literature results,[5] EBSD clearly showed that the investigated KB was intergranular, at least in its inclined part (Figure 4). Detailed imaging showed that despite the high voltage and working distance used, EBSD analysis did not miss fine grains close to the KB. Grains surrounding the KB were selected for texture analysis (Figures 4(d) and (e)). Despite their low number (88), they exhibited a fairly uniform texture, both from their {100}, {110}, and {111} pole figures and from the calculation of their orientation distribution function. This is illustrated by the {001} pole figure in Figure 4(f). No particular grain boundary misorientation was either found close to the KB. Tiny bright particles, up to 0.5 μm in size, were found along the KB (Figure 4(c)). The particle size was higher than that reported by Sato *et al.*[17] in a JLR of a 5052 aluminum alloy but similar to that reported in Reference 5 for a JLR of a 1050 aluminum alloy. The presence of a continuous film, less than 100 nm in thickness, as reported in Reference 5 could not be detected in the SEM. However, no particular contrast was observed along the KB between the particles, suggesting a local chemical composition close to that of the alloy and not strongly enriched in oxygen. The size of the particles in Figure 4 is much higher than the typical thickness of the native oxide layer on aluminum alloys (a few nanometers[41]). This suggests that oxide particles are not the result of
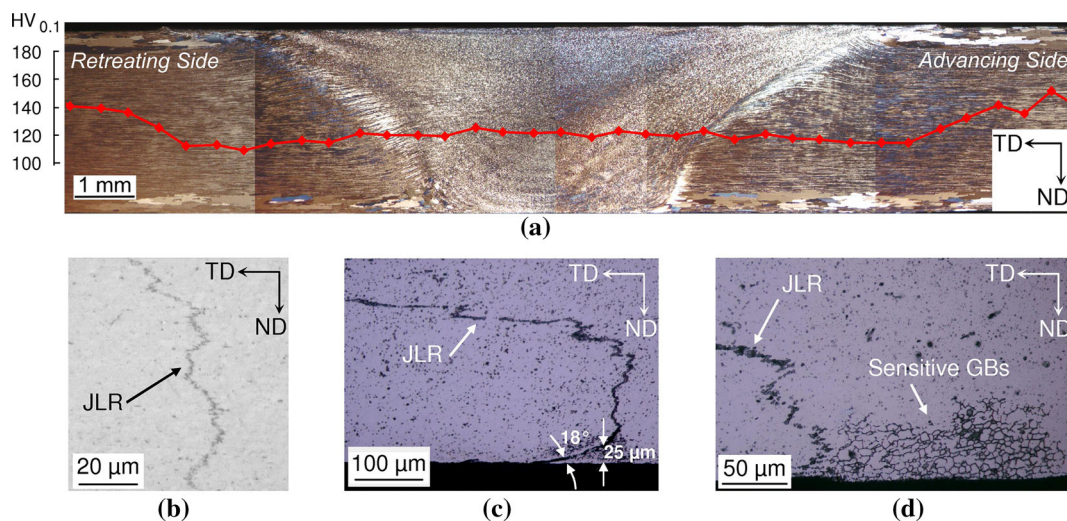

(a)

(b)

(c)

(d)

Fig. 3—Light optical micrographs of the investigated welds. (*a*) General view (anodic oxidation) and hardness profile across the top part of the weld; (*b*) JLR feature close to the mid-thickness (full etching procedure); (*c*) KB emerging at the nugget root (full etching procedure); (*d*) "sensitive GBs" in a Gap0.3 weld, close to the nugget root (full etching procedure). The lower surface of the sheets is on bottom of all images.
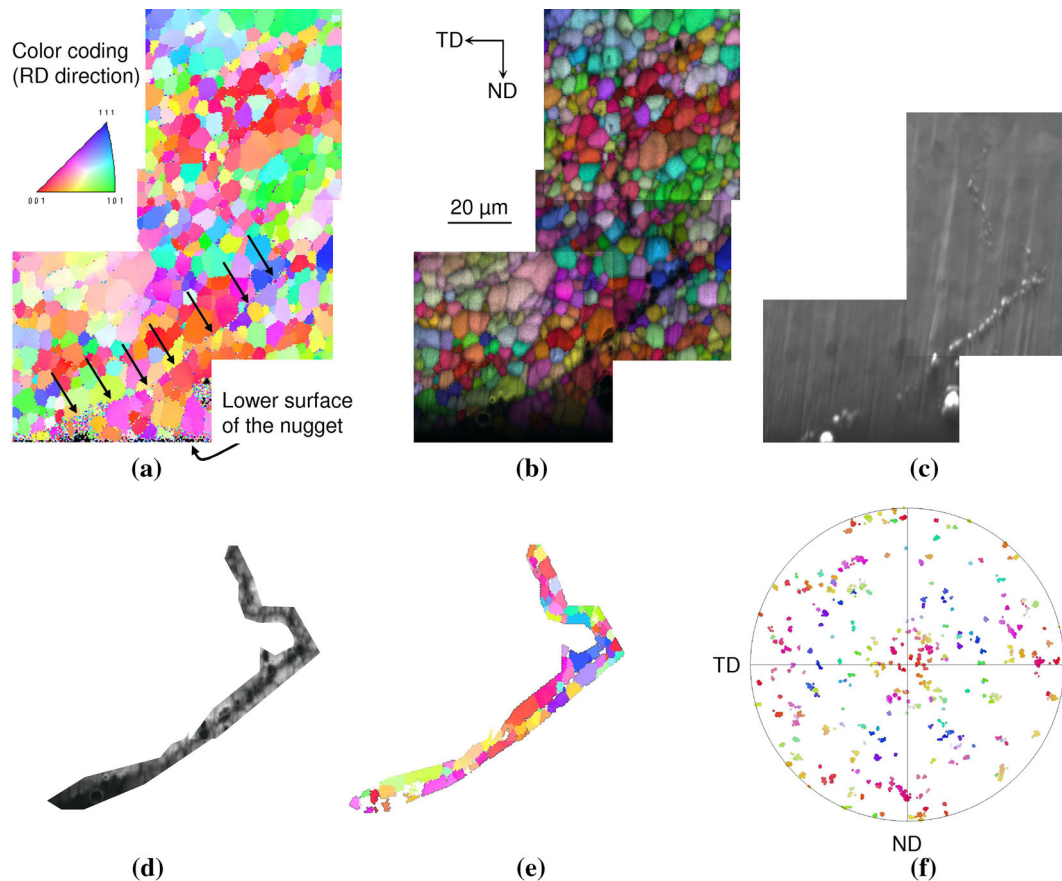
Fig. 4—EBSD map (raw data) of a KB (indicated with arrows) in cross section close to the nugget root. (*a*) Orientation of RD with respect to the crystals; (*b*) same as (a) but combined with the quality of EBSD patterns (in gray levels) to better reveal grain boundaries and the KB flaw; (*c*) electron image after tilt correction, showing bright particles at the KB only; (*d*, *e*) grains neighboring the KB and selected to plot the {001} pole figure as shown in (*f*). (d) Same gray shading as in (b); (e, f) same color coding as in (a).

breaking the native oxide layers of faying surfaces during welding. The thermal–mechanical cycle experienced by native oxide is nevertheless at the origin of the KB and JLR features, as those were not observed in "sound welds" of this study, which were made from seamless material. The physical mechanisms leading to formation of oxide particles, starting from a much thinner oxide layer, are still unknown.

The "Gap" welds evidenced a region close to (but not necessarily at) the nugget root where grain boundaries seemed to be more sensitive to the chemical etching procedure (Figure 3(d)). STEM analysis revealed some grain boundary regions enriched in copper (Figures 5(a) and (b)) as well as oxygen-rich precipitates (Figures 5(c) and (d)). This indicates significant metallurgical changes with respect to gap-free welds, although such regions (referred to as "sensitive GBs" hereafter) did not lead to any lower hardness values or difference in grain size. Such grain boundary films enriched with alloying elements have already been reported[42] in a 7010-T651 alloy after FSW. Their presence was attributed to local dissolution of precipitates, followed by incipient melting by eutectic reactions at grain boundaries. It may even lead to liquation cracking after welding of dissimilar aluminum alloys.[43,44] In contrast with these findings, no crack was observed in "sensitive GBs" before tensile testing. Moreover, "sensitive GBs" were observed close to the bottom surface of the welds only, whereas incipient melting was reported to occur mainly close to the top surface or the welds. A possible explanation is that the chemical composition close to the grain boundaries did not allow reaching the melting point under the conditions used in this study. Other metallurgical phenomena in relation with the thermo-mechanical cycle locally encountered during welding in this region might also have occurred during stirring of "Gap" welds that could strongly differ from those reported by[42–44] in the case of gap-free welds. Nevertheless, the higher copper content found in "sensitive GBs" suggests that copper-rich precipitates might have dissolved at GBs during the welding cycle.[42–44]

B. Tensile Properties of the Base Metal

Tensile properties of the base metal are reported in Figure 6(a) and Table I. The yield strength, work-hardening behavior, tensile strength, and Lankford coefficients are anisotropic. The much lower strength along DD has commonly been observed in Al-Cu-Li alloys in the T8 state.[45–47] The tensile curves are very similar to those reported by Chen *et al.*[47] in a 2198-T8 alloy but show higher strength than those reported by Ma *et al.*[48] The
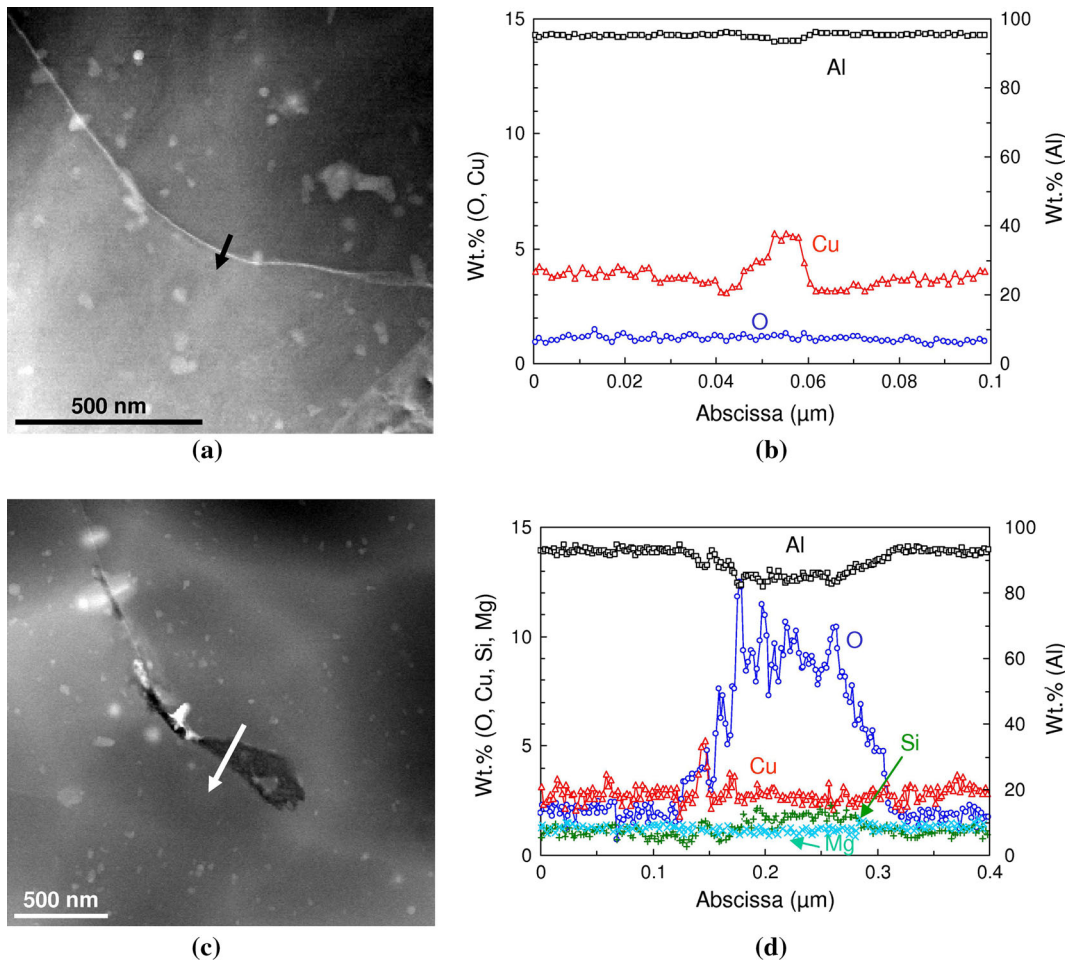
(a)

(b)

(c)

(d)

Fig. 5—(*a*) and (*c*) STEM-HAADF micrographs of "sensitive GBs" in a Gap0.7 weld. Contrast in both images is dominated by the mean atomic number, Z (Z-contrast). STEM-EDX analysis (*b*) across a grain boundary enriched in copper, along arrow in (a), and (*d*) across an oxygen-rich particle, along arrow in (c). The high ground level of oxygen might stem from some the native oxide layer of the thin foil.

values of Lankford coefficients, however, significantly differ from those published by.[45,47] Ductile fracture occurred after necking, and the gauge region encompassing the necking region fully (*e.g.*, specimen tested along DD in Figure 6(a)) or only partly (specimens tested along TD and TD in Figure 6(a)) from one test to another.

C. Tensile Behavior of the Cross-Weld Specimens

From Figure 6 and Table II, "sound," JLR-bearing, and KB-bearing welds exhibit similar tensile properties. They differ in strength by less than 6 pct compared with "sound" welds. Their yield strength (resp. tensile strength) is slightly higher than those reported by Ma *et al.*[48] for 2-mm-thick 2198-T8 FSW joints. It is driven by that of the weld nugget (Table I), being lower by 40 pct (resp. 20 pct) than that of the base metal along the same direction. The resulting efficiency ratio is about 80 pct, similar to that reported by Denquin *et al.*[40] for a 2098-T8 FSW joint. It falls within the range 70 to 90 pct commonly reported in the literature for alloys welded in the heat-treated condition.[8,30,31,39,40,49–52] The strength of "Gap" welds is slightly lower than that of the other cross-weld specimens.

Reconstructed strain fields are illustrated in Figure 7 for an elongation of 15 pct (gauge length 14 mm). They showed no significant difference between the different types of welds, except for the Gap0.7 specimen, for which the axial engineering strain appeared slightly more homogeneously distributed. Note, however, that the size of the KB was too small for strain localization to be reliably detected there with the selected experimental setup. Strong strain localization occurred at the macroscopic scale close to the TMAZ/HAZ boundary, as commonly reported in the literature (*e.g.*,[53,54]).

D. Fracture Mode and Fracture Mechanisms of Tensile Specimens

For all cross-weld specimens, failure occurred abruptly by ductile fracture after strain localization. Crack initiation and propagation regions were determined from both fracture surface and cross-section observations of all tested specimens, and are also reported in Table II. Typical fracture surfaces (Figure 8) exhibit dimples in the nugget and mixed dimpled/ "fibrous" fracture (*i.e.*, exhibiting some intergranular features) for the base metal pulled in tension along TD,
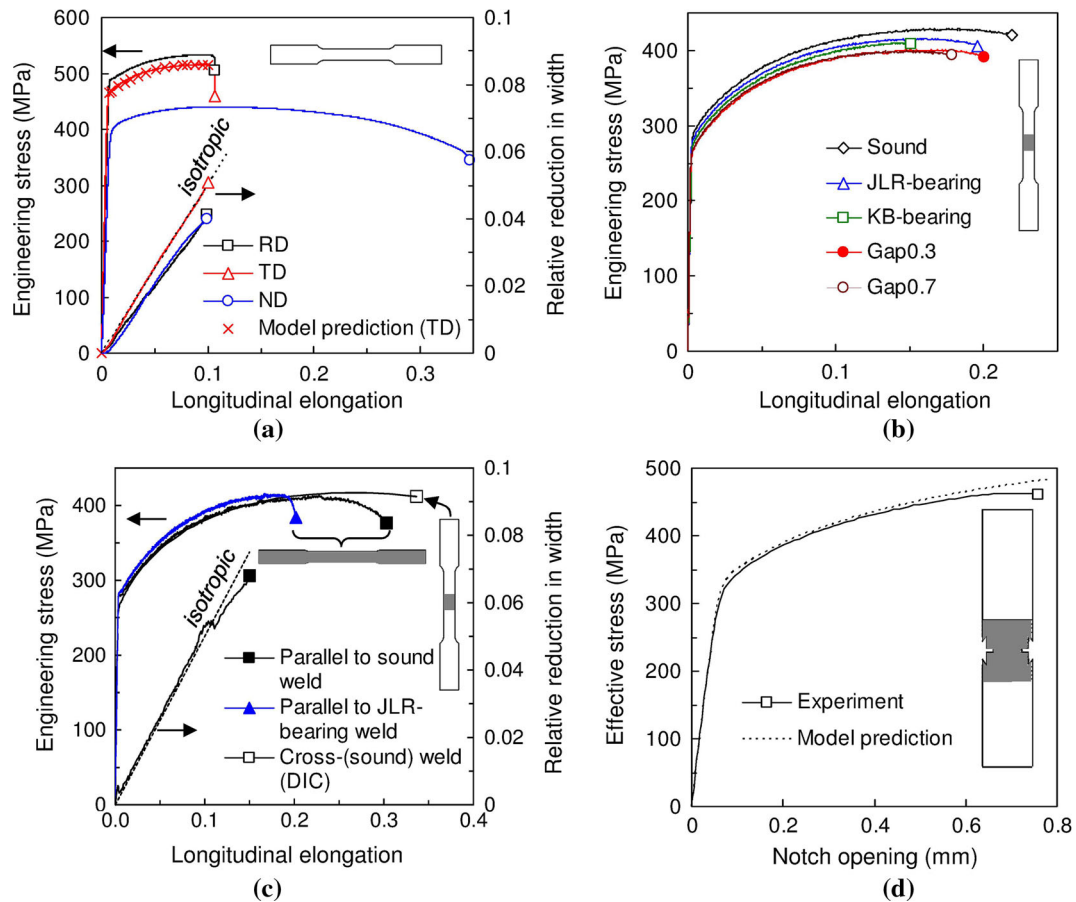
Fig. 6—Tensile curves (*a*) of the base metal; (*b*) of cross-weld specimens (sound weld, gauge length: 14 mm); (*c*) of the nugget, loaded parallel to the weld direction; (*d*) of a cross-weld specimen notched within the nugget (sound weld).

Table I. Average Uniaxial Tensile Properties of the 2198-T851 Base Metal and of the Weld Nugget

Material	0.2 pct Proof Stress (MPa)	Tensile Strength (MPa)	Max. Uniform Elongation (Gauge Length: 14 mm)	Lankford Coefficient, r (Elongation Between 0 and 0.1)
Base metal (//RD)	490	530	10.0	0.80
Base metal (//TD)	470	515	10.0	1.05
Base metal (//DD)	400	445	12.6	0.80
Weld nugget (//welding direction)	284	413	16.2	1.10

as already reported by Chen *et al*.,[47] and TMAZs. In agreement with[1,8,50,55] but in contrast to,[56] the JLR feature did not interact with damage mechanisms in the considered welded joints. The scatter in tensile elongation illustrated in Figure 6 between different kinds of welds is similar to that observed between specimens cut from the same welded joint.

The striated, locally ductile fracture at the weld root of KB specimens (Figure 8(c)) is consistent with a lack of mixing between the two sheets, leaving an intergranular oxide film along the KB. The local ductility, however, suggests that this film might be non-continuous in three dimensions, in contrast to the literature results from thin foil observations.[5] In contrast, it is consistent with SEM observations reported in the current study. The orientation of fracture surfaces (tilted close to the nugget root and then approximately

flat over about 100 μm) is also consistent with the KB geometry (Figure 3(c)). The crack then leaves the KB and further propagates into the weld nugget. Such fracture initiation at the KB has already been reported for some (but not all) FSW joints.[11]

The "sensitive GBs" of Gap0.3 welds did not interact with fracture mechanisms: no damage was detected in the weld nugget after fracture. In Gap0.7 welds, however, fracture initiates intergranularly from "sensitive GBs" (Figure 8(d)). The apparent roughness of grain boundary facets might be due to nanometer-sized dimples, revealing local softening and/or heavy strain localization at (or very close to) grain boundaries. Consistently with,[57] a clearance of 10 pct of the parent sheet thickness may be high enough to induce a decrease in strength of the weld. A clearance of 23 pct of the parent sheet thickness is high enough, in the investigated

Table II. Tensile Properties of the Welded Joints

Welds	YS (MPa)	TS (MPa)	Elongation at TS (pct) (Gauge Length: 14 mm)	Efficiency Ratio (pct) (*i.e.*, of TS to that of Base Metal)	Average Axial Strain for an Overall Axial Strain of 15 pct (Gauge Length 14 mm)			Fracture Locus
					TMAZ (AS)	Weld Nugget	TMAZ (RS)	
Sound	282 to 302	412 to 429	19.5 to 22.4	80 to 83	20	15	22	TMAZ (RS)
JLR- bearing	285 to 296	413 to 416	15.7 to 17.5	80	20	15	25	TMAZ (RS) in two cases, TMAZ (AS) in one case
KB-bearing	265 to 287	398 to 410	14.2 to 19.5	77 to 80	22	20	25	weld nugget, starting from KB
Gap0.3	282 to 284	401 to 404	16.9 to 17.3	78	20	13	25	TMAZ (RS), propagation into the nugget
Gap0.7	277 to 281	398 to 399	14.8 to 15.4	77	19	19	22	weld nugget, starting from "sensitive GBs"

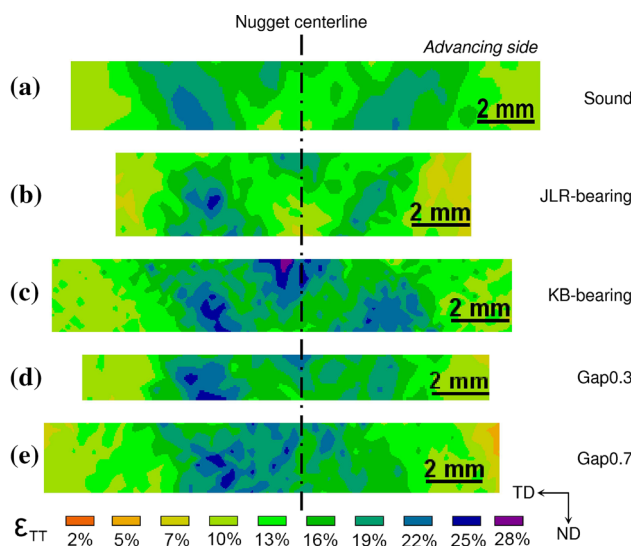AS: advancing side; RS: retreating side.

Fig. 7—Reconstructed axial elongation fields (side edge) for an average elongation of 15 pct (over a gauge length of 14 mm). (*a*) Sound; (*b*) JLR-bearing; (*c*) KB-bearing; (*d*) Gap0.3; (*e*) Gap0.7 weld. The center of the nugget is indicated with a dashed line.

conditions, to trigger intergranular crack initiation and propagation from the nugget root. This is lower than the threshold value reported by Oki *et al.*[58] (about 50 pct of the parent sheet thickness of 3 mm), yet determined for a fairly different material (AA5083-O alloy). The reason why "sensitive GBs" in Gap0.3 welds were less sensitive to fracture than those of Gap0.7 welds is still unknown but may be related to the size of "sensitive GBs" regions being larger in the case of the Gap0.7 welds (40 μm of height against 20 μm for the Gap0.3 welds). Comparative TEM investigation of these two regions might be helpful to address this issue.

E. Toward a Crack Initiation Criterion for the Kissing Bond

Crack initiation at KB or at "sensitive GBs" does not seem to significantly impair tensile properties (Figure 6 and Table I). However, it could be highly detrimental to the fatigue lifetime. A fracture criterion of KB was thus determined from *in situ* tensile tests in the SEM. Due to the low stiffness of the tensile stage, only the crosshead displacement (instead of axial elongation of the specimen) is reported in Figure 9. The case of "sensitive GBs" was not addressed in the current study, since such a gap could possibly be more easily detected during the welding process than formation of a KB flaw. Strain localization close to the KB (at specimen surface), possibly due to subsurface cracking of the KB, appeared for an engineering stress of about 260 MPa as indicated by black arrows. A surface crack was observed from place to place for an engineering stress of 280 MPa, as indicated by white arrows. They were linked by a linear feature (indicated with empty arrows). This suggests strong strain localization after subsurface cracking. Upon further loading, the crack eventually reached the observed surface of the specimen. Cracking of the KB is clearly discontinuous, as confirmed by the strong heterogeneity in crack tip opening displacement detected from microtomography observations (Figure 10). The roughness of the crack mouth observed in microtomography images is consistent with the grain size close to the KB, which again suggests intergranular cracking along the KB itself. From these results, a threshold stress of 260 MPa was taken as a phenomenological fracture crack initiation criterion at the KB, although the fracture micromechanism could be actually driven by strain localization (and not by stress) at a very local scale. This criterion is to be used to interpret fatigue failure modes of the same KB-bearing welds. It is only valid for the welding conditions that were used here, as
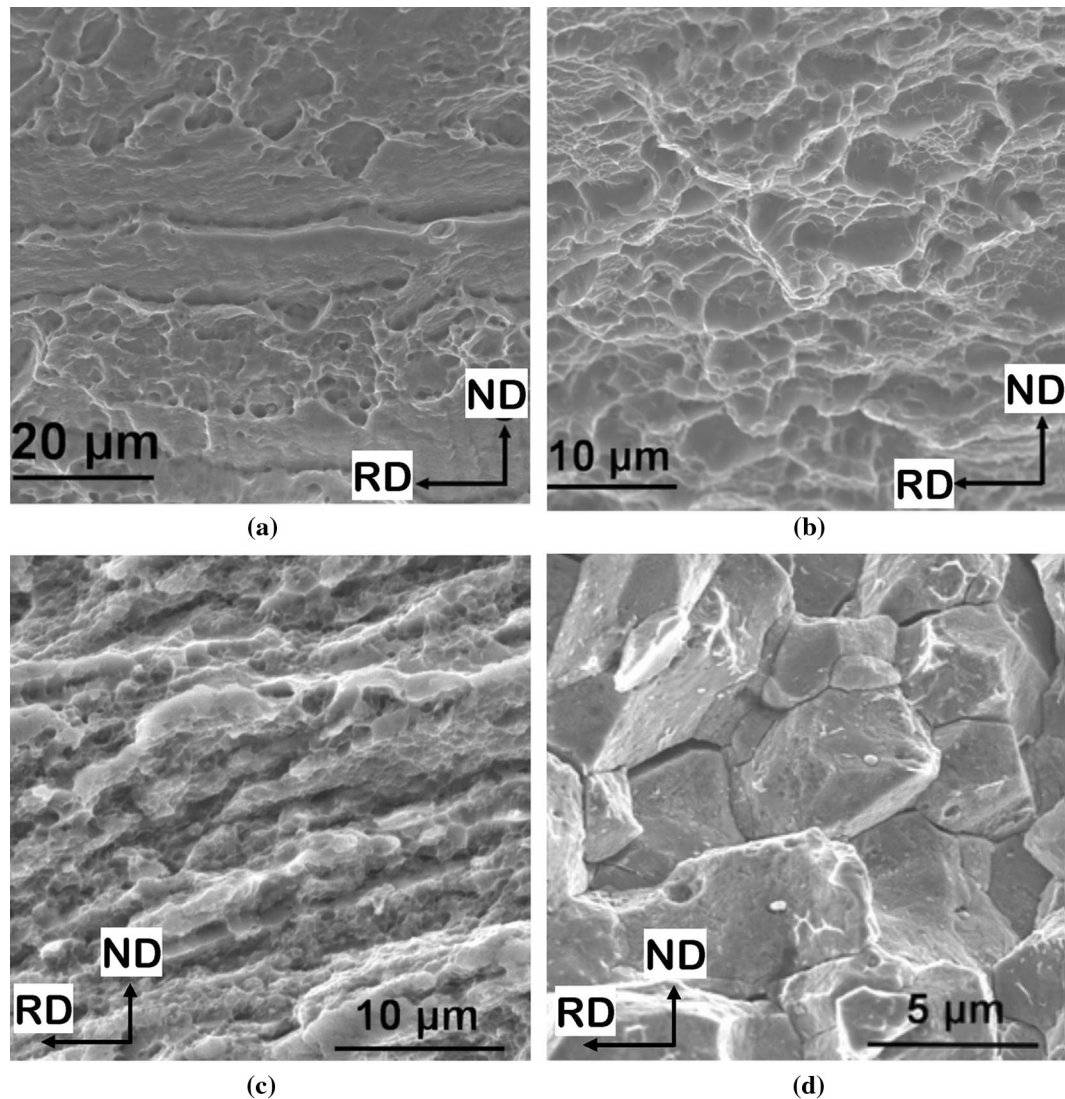
Fig. 8—Typical fracture surfaces of cross-weld specimens. (*a*) Mixed dimpled/fibrous fracture (TMAZ); (*b*) dimpled fracture of small, equiaxed grains in the nugget; (*c*) ductile (submicrometer-dimpled) fracture along the KB; (*d*) intergranular fracture along ''sensitive GBs'' of a Gap0.7 specimen.

residual stresses were not explicitly taken into account in the current study. Nevertheless, the onset of cracking was only detected after large scale plastic yield of the nugget. As a result, residual stresses might have redistributed at least locally before opening of the KB.

IV. MODELING THE ELASTOPLASTIC YIELD BEHAVIOR OF THE WELDED JOINTS

According to the similarity of their macroscopic behavior, all welded joints were represented using a unique three-dimensional (3D) multi-material model. Residual stresses were not explicitly taken into account in the following but implicitly integrated into the constitutive model. Consequently, the following results cannot be directly transposed to other sheet geometry or welding conditions.

Following an approach similar to that of *e.g.*,[49,54,59,60] the welded joints were artificially divided

into several ''materials'' after the axial elongation map of a sound weld loaded up to an average axial elongation of 15 pct. It has already been shown in several aluminum alloys that using strain fields inferred from digital image correlation could yield reliable results compared with performing tensile tests on miniature specimens cut from the different zones.[60] Seven zones were distinguished as follows (Figure 11):

- The weld nugget was modeled according to the tensile curves of Figures 6(c) and (d);
- The TMAZs were separately modeled for the advancing and retreating sides, respectively;
- To simply take the hardness gradient (Figure 3(a)) into account, the HAZ of either side was cut into three parts (HAZ-1, HAZ-2, and HAZ-3, respectively) according to strain field monitoring results. For the sake of simplicity, the behavior of the corresponding HAZ regions at either side of the weld was considered to be unique.

- The base metal was modeled according to its tensile curve along TD, *i.e.*, parallel to the loading direction of cross-weld specimens.

The constitutive behavior of the considered zones was identified using available experimental information,
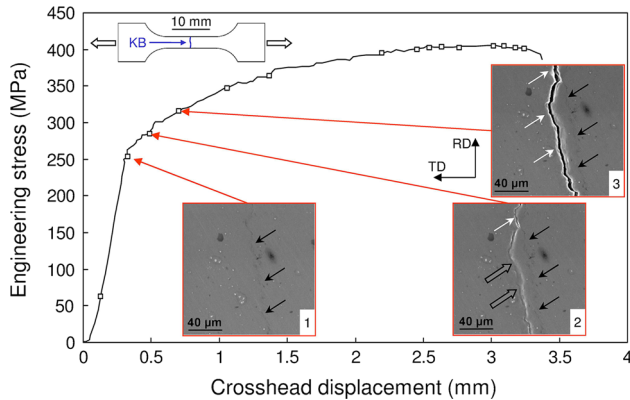

Fig. 9—Results of an *in situ* tensile test: engineering stress *vs* displacement curve and selected secondary electron images of the bottom surface of the weld: strain localization (stage 1), then surface crack initiation (stage 2) and opening (stage 3) at the KB, close to the mid-width of the weld. Interruptions of the test are indicated with squares. Linear feature delineated by black arrows is thought to be subsurface cracks. Surface cracks (delineated by white arrows) are linked by regions with strong localization of strain, delineated by empty arrows.

including full 3D calculation of the specimen. Linear 8-node linear brick elements with reduced integration were used in the in-house Z-set finite element code,[61] together with an implicit integration scheme. Symmetry conditions were applied to the mid-width, and prescribed displacement was applied along the tensile axis. The mesh size was close to the size of the regions of interest used in DIC data processing (*i.e.*, 0.24^2 mm^2) in the plane observed during the test and about 1 mm along the specimen width. Identical results were obtained with a mesh size two times finer. As a result, convergence of model predictions with respect to the mesh size was considered to be satisfactory.

A. Constitutive Equations

The elastoplastic behavior of a given region, Ω, was represented using homogeneous and isotropic elastic properties (characterized by unique values of Young's modulus and Poisson ratio), a von Mises yield criterion together with non-linear isotropic hardening (Voce-type evolutionary equation) as follows:

$$f_\Omega(\underline{\sigma}) = \sigma_{eq} - R = \sigma_{eq} - \left(R_{0-\Omega} + Q_\Omega\left(1 - e^{-b_\Omega p}\right)\right) \quad [1]$$

In Eq [1], σ_{eq} is the von Mises equivalent stress, $\underline{\sigma}$ is the local tensile stress tensor, and p is the cumulative plastic strain (determined using a von Mises equivalent). Constitutive parameters $R_{0-\Omega}$, Q_Ω, and b_Ω were determined for each region of the specimen (Table III) as
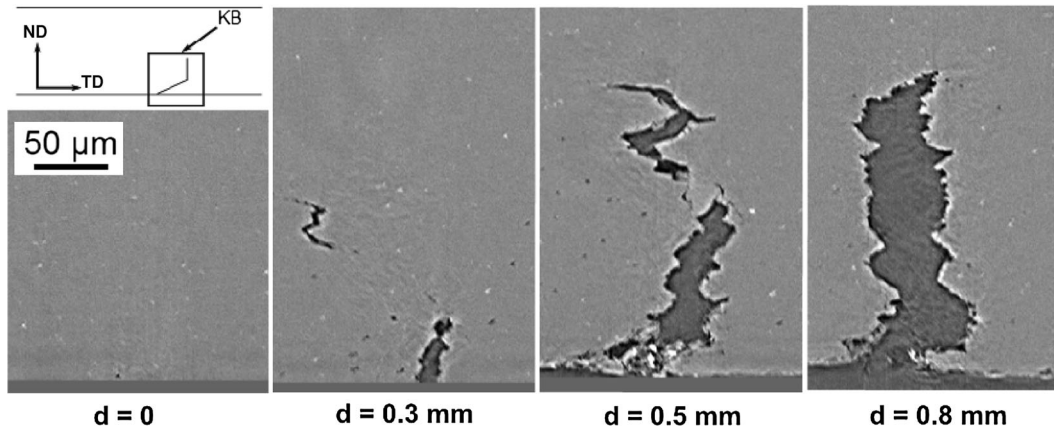

Fig. 10—2D slices at different locations (*d*: distance from top slice) along the weld line of the reconstructed 3D image obtained by microtomography after pulling the KB-bearing cross-weld specimen in uniaxial tension up to an engineering stress of 380 MPa. The loading axis is horizontal.
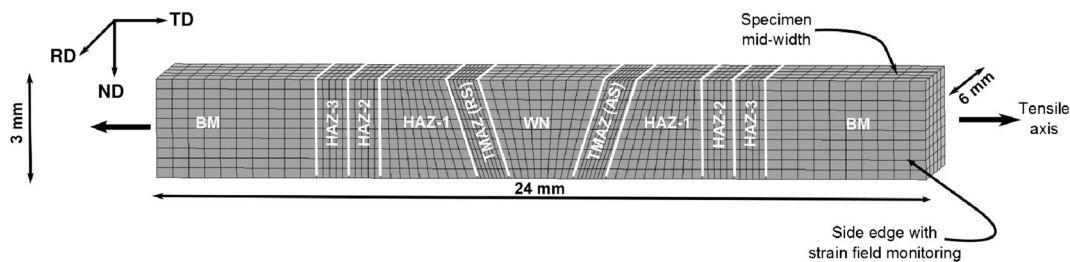

Fig. 11—3D mesh of one-half of the gauge part of cross-weld specimens, showing the considered zones. (WN, weld nugget; AS, advancing side; RS, retreating side).

described below. The normality rule was applied to determine the evolution of plastic strain.

B. *Determination of Constitutive Parameters*

Although the plastic behavior of the base metal was experimentally determined to be anisotropic, only the tensile curve corresponding to loading along TD was used. Note that from Table I and Figure 6(a), the Lankford coefficient along direction TD is very close to 1. This assumption is thus expected to only little influence strain localization in the specimen, as softer regions (TMAZ and weld nugget) are located rather far from the base metal. Good agreement between experimental measurements and model predictions was obtained (Figure 6(a)).

Constitutive parameters of the weld nugget were determined using the uniaxial tensile curve of Figure 6(c)

from the specimen cut along the "sound" nugget. In fact, the three curves (along both nuggets and from the cross-weld specimen) are close to each other, when considering the experimental scatter, *e.g.*, Table II. Three-dimensional numerical simulation of the test on notched specimens (mesh size at notch root: 50 μm) loaded along TD predicted a load *vs* notch opening curve in good agreement with experimental data (Figure 6(d)) and confirmed that plastic deformation only occurred within the weld nugget. Together with the Lankford coefficient close to 1 for an elongation up to 0.1 (Figure 6(c)), this shows that an isotropic yield assumption may be considered as reasonable in this simple constitutive model of the weld nugget.

No experimental data were available to directly determine the constitutive parameters of TMAZ and HAZ regions. As in Reference 59, 60, a first approximation of the uniaxial tensile behavior of these regions along TD

Table III. Optimized Sets of Constitutive Parameters (For all Regions, Young's Modulus: 74 GPa; Poisson Ratio: 0.3)

Region, Ω	Weld Nugget	TMAZ (RS)	TMAZ (AS)	HAZ-1	HAZ-2	HAZ-3	Base Metal//TD
$R_{0-\Omega}$ (MPa)	281	243	270	275	280	310	463
Q_{Ω} (MPa)	272	600	385	270	320	230	128
b_{Ω}	8.9	1.2	1.8	19.5	37.6	65.3	18.0

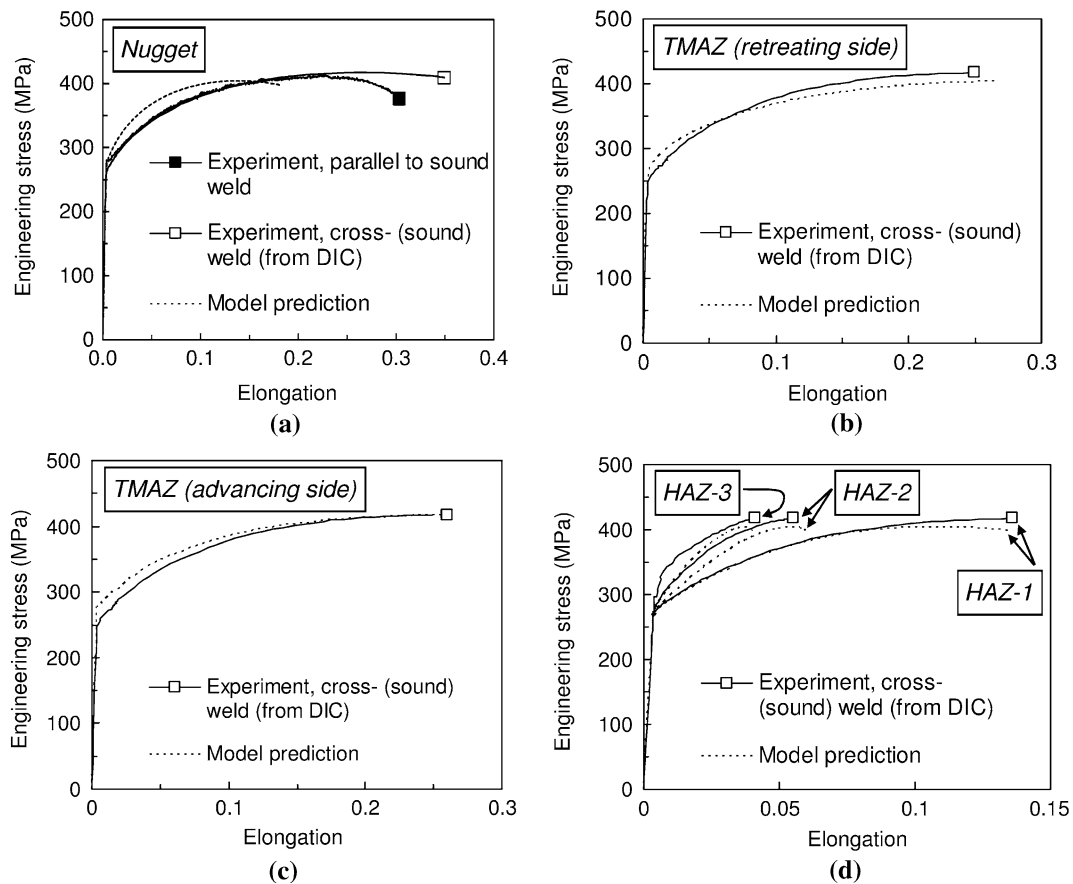RS: retreating side; AS: advancing side.

Fig. 12—Comparison between experimental and predicted values of mid-thickness axial elongation, ε_{Ω}, for various regions in the cross-weld specimen.
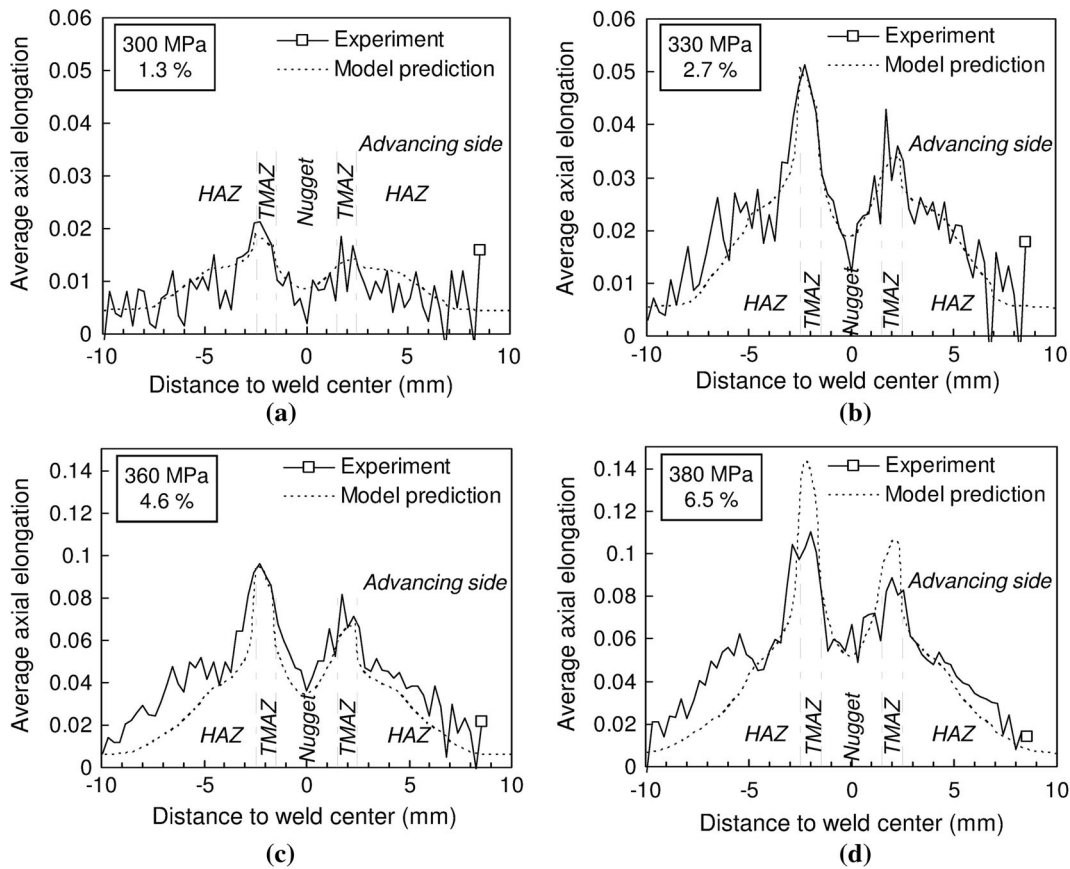
Fig. 13—Measured and predicted axial elongation at the side edge (mid-thickness) of a "sound" cross-weld specimen.

was made by averaging the axial engineering strain measured at mid-thickness in the considered region, ε_Ω, and plotting the applied engineering stress vs ε_Ω. Only data at the advancing side were considered to determine constitutive parameters for the three HAZ regions. A preliminary set of constitutive parameters was determined for each region using these curves. Fine tuning of constitutive parameters was then made using 3D numerical simulation of the full structure (Figure 11). In view of the modeling assumptions, good agreement was obtained between experimental and predicted stress–strain curves for the different regions of the weld (Figure 12).

C. Comparison Between Measured and Predicted Strain Fields

Good agreement was obtained between measured and predicted macroscopic tensile curves: the difference in strength was lower than 1 pct up to an engineering stress of 400 MPa (average elongation of 11 pct). For an average elongation higher than 11 pct, premature strain localization was predicted with the model. Estimates of the stress state using the model could thus be made only up to an average elongation of 11 pct. This value is high enough for the analysis of fatigue strength data for the targeted lifetime of components (around 10^5 cycles).[24] Predicted axial elongation profiles (side edge, mid-thickness) were calculated on the basis of displacement between consecutive nodes. They were compared with

experimental results obtained on the basis of elongation between consecutive centers of DIC regions of interest. The averaging process used here does not allow revealing strain discontinuities across interfaces. Nevertheless, this comparison makes sense because the size of finite elements and that of DIC regions of interest are very similar. Good agreement between experimental and predicted profiles was obtained up to an engineering stress of about 360 MPa, both in localization of severely deformed regions and in local values of axial elongation (Figure 13). Agreement is slightly less satisfactory for the HAZ regions at the retreating side, due to the simplifying assumption of identical properties in the HAZ at either side of the weld.

Strain localization within the TMAZ is both qualitatively and quantitatively predicted with the model up to about 4.6 pct of elongation. The stress triaxiality ratio, τ, i.e., the ratio between the von Mises equivalent stress and the hydrostatic stress, was estimated using the model for an average elongation (over the gauge region) of about 15 pct. Its value stayed close to 1/3 except in the TMAZ where strain localization and constraint by the stronger surrounding regions induced a marked increase in τ up to about 2/3 at mid-width. In addition to strain acceleration, such high values of stress triaxiality could strongly favor ductile damage development by void growth which will again contribute to the local softening of the material. This might explain why fracture occurs abruptly in the TMAZ in many of the tested cross-weld specimens.

Within the nugget, the stress triaxiality remains close to one-third, and the axial stress remains close to the applied stress. The loading conditions of the weld nugget thus remain close to uniaxial tension, despite structural effects induced by the multi-material character of the welded joints. This result is a starting point for the analysis of fatigue test data on cross-weld specimens.

V. CONCLUSIONS

Microstructural and mechanical characterization of base material, "*sound*" (bead-on-plate) and flaw-bearing (*joint line remnant, kissing bond,* and *gap*) FSW butt joints of as-welded AA2198-T851 alloy lead to the following conclusions:

In terms of *plastic tensile behavior,* the yield strength of the welds is reduced by 40 pct and the UTS by 20 pct compared with the base material. The macroscopic stress–strain response is hardly affected by the presence of the flaws compared with the sound welds. From strain field measurements on the butt surface, strain localization in the TMAZ at the retreating side is evidenced for the welds, except for the "gap" welds where plasticity is more homogeneous over the different weld zones. A 3D finite element model of a sound weld has been created using different elastic–plastic constitutive parameters for the different zones identified by digital image correlation. It manages to reproduce the strain profiles and macroscopic weld response in good agreement with the experiment. *Failure* location is sensitive to the presence of some (but not all) of the considered weld flaws.

The detailed results for the different weld flaws are as follows:

1. EBSD revealed that the *kissing bond* is an intergranular feature, which opened under a normal stress of about 260 MPa during an *in situ* SEM tensile test. The discontinuous opening and the rough morphology of the opened KB could be revealed by synchrotron radiation tomography. Its fracture mechanism might involve nanometer-sized dimples created at the interface between the metal and a discontinuous oxide film. The kissing bond acts as crack initiation site for final fracture of the tensile specimen.
2. Leaving a *gap* of at least 10 pct of the sheet thickness results in a region where grain boundaries are more sensitive to metallographic etching. From TEM analysis, such boundaries exhibit oxygen-rich nanometer-sized particles and/or enrichment in copper. Intergranular fracture of these zones occurs for a gap equal to 23 pct of the sheet thickness, followed by crack propagation into the weld nugget leading to final fracture.
3. "*Sound*" joints, joints with a *joint line remnant* or a *gap* of only 10 pct of the sheet thickness, exhibited abrupt ductile fracture from strain localization in one of the softer TMAZs.
4. The above results are considered as a starting point to analyze the fatigue lifetime of the same flaw-bearing FSW welded joints.

REFERENCES

1. P.L. Threadgill, A.J. Leonard, H.R. Shercliff, and P.J. Withers: *Int. Mater. Rev.*, 2009, vol. 54, pp. 49–93.
2. R.Q. Yu, B. Hu, and H.C. Zou: *Sci. Technol. Weld. Join.*, 2012, vol. 17, pp. 534–38.
3. M.-S. Han, S.-J. Lee, J.-C. Park, S.-C. Ko, Y.-B. Woo, and S.-J. Kim: *Trans. Nonferrous Met. Soc. China*, 2009, vol. 19, pp. S17–22.
4. S.-O. Yoon, M.-S. Kang, H.-B. Nam, Y.-J. Kwon, S.-T. Hong, J.-C. Kim, K.-H. Lee, C.-Y. Lim, and J.-D. Seo: *Trans. Nonferrous Met. Soc. China*, 2012, vol. 22, pp. S619–23.
5. Y.S. Sato, H. Takauchi, S.H.C. Park, and H. Kokawa: *Mater. Sci. Eng. A*, 2005, vol. A405, pp. 333–38.
6. S. Di, X. Yang, G. Luan, and B. Jian: *Mater. Sci. Eng. A*, 2006, vols. A435–436, pp. 389–95.
7. H.B. Chen, K. Yan, T. Lin, S.B. Chen, C.Y. Jiang, and Y. Zhao: *Mater. Sci. Eng. A*, 2006, vol. A433, pp. 64–69.
8. Y. Uematsu, K. Tokaji, H. Shibata, Y. Tozaki, and T. Ohmune: *Int. J. Fatigue*, 2009, vol. 31, pp. 1443–53.
9. T. Le Jolu, T.F. Morgeneyer, and A.F. Gourgues-Lorenzon: *Sci. Technol. Weld. Join.*, 2010, vol. 15, pp. 694–98.
10. L. Cui, X. Yang, G. Zhou, X. Xu, and Z. Shen: *Mater. Sci. Eng. A*, 2012, vol. A543, pp. 58–68.
11. T.L. Dickerson and J. Przydatek: *Int. J. Fatigue*, 2003, vol. 25, pp. 1399–1409.
12. A.J. Leonard and S.A. Lockyeri: *Proc. 4th International Symposium on Friction Stir Welding*, The Welding Institute, Great Abington, Cambridge (paper on CD-ROM), 2004.
13. T. Vugrin, M. Schmücker, and G. Stanieki: *Proc. Symposium on Friction Stir Welding and Processing III*, San Francisco, CA, K.V. Jata, M.W. Mahoney, R.S. Mishra, and T.J. Lienert, eds., TMS, Warrendale, PA, 2005, pp. 277–84.
14. C. Zhou, X. Yang, and G. Luani: *Mater. Sci. Eng. A*, 2006, vol. A418, pp. 155–60.
15. B. Li, Y. Shen, and W. Hu: *Mater. Des.*, 2011, vol. 32, pp. 2073–84.
16. F. Palm, H. Steiger, and U. Henneböhle: *Proc. 4th International Symposium on Friction Stir Welding*, The Welding Institute, Great Abington, Cambridge, UK (paper on CD-ROM), 2004.
17. Y.S. Sato, F. Yamashita, Y. Sugiura, S.H.C. Park, and H. Kokawa: *Scripta Mater.*, 2004, vol. 50, pp. 365–69.
18. B.C. Liechty and B.W. Webb: *J. Mater. Proc. Technol.*, 2007, vol. 184, pp. 240–50.
19. B.C. Liechty and B.W. Webb: *J. Mater. Proc. Technol.*, 2008, vol. 208, pp. 431–43.
20. J.-Q. Su, T.W. Nelson, R. Mishra, and M. Mahoney: *Acta Mater.*, 2003, vol. 51, pp. 713–29.
21. J.-Q. Su, T.W. Nelson, and C.J. Sterling: *Mater. Sci. Eng. A*, 2005, vol. A405, pp. 277–86.
22. J.-Q. Su, T.W. Nelson, and C.J. Sterling: *Philos. Mag.*, 2006, vol. 86, pp. 1–24.
23. K. Inada, H. Fujii, Y.S. Ji, Y.F. Sun, and Y. Morisada: *Sci. Technol. Weld. Join.*, 2010, vol. 15, pp. 131–36.
24. T. Le Jolu, T.F. Morgeneyer, A. Denquin, and A.F. Gourgues-Lorenzon: *Int. J. Fatigue*, DOI:10.1016/j.ijfatigue.2014.07.001, Accepted.

25. Y.G. Kim, H. Fujii, T. Tsumura, T. Komazaki, and K. Nakata: *Mater. Sci. Eng. A*, 2006, vol. A415, pp. 250–54.

26. K. Chung, W. Lee, D. Kim, J. Kim, K.-H. Chung, C. Kim, K. Okamoto, and R.H. Wagoner: *Int. J. Solids Struct.*, 2010, vol. 47, pp. 1048–62.

27. M. Abbasi Gharacheh, A.H. Kokabi, G.H. Daneshi, B. Shalchi, and R. Sarrafi: *Int. J. Mach. Tools Manuf.*, 2006, vol. 46, pp. 1983–87.

28. F. Hild, J.N. Perie, and M. Coret: Internal Report No. 230, LMT-Cachan, France (in French), 1999.

29. F. Hild, B. Raka, M. Baudequin, S. Roux, and F. Cantelaube: *Appl. Opt.*, 2002, vol. 41, pp. 6815–28.

30. B. Heinz and B. Skrotzki: *Metall. Mater. Trans. B*, 2002, vol. 33B, pp. 489–98.

31. M. Ericsson and R. Sandström: *Int. J. Fatigue*, 2003, vol. 25, pp. 1379–87.

32. C. Genevois: Ph.D. Dissertation, Institut National Polytechnique de Grenoble, France, 2004 (in French).

33. W. Woo, H. Choo, D.W. Brown, S.C. Vogel, P.K. Liaw, and Z. Feng: *Acta Mater.*, 2006, vol. 54, pp. 3871–82.

34. C. Gallais, A. Denquin, Y. Bréchet, and G. Lapasset: *Mater. Sci. Eng. A*, 2008, vol. A496, pp. 77–89.

35. P.M.G.P. Moreira, F.M.F. de Oliveira, and P.M.S.T. de Castro: *J. Mater. Proc. Technol.*, 2008, vol. 207, pp. 283–92.

36. C.G. Derry and J.D. Robson: *Mater. Sci. Eng. A*, 2008, vol. A490, pp. 328–34.

37. Y.E. Ma, P. Staron, T. Fischer, and P.E. Irving: *Int. J. Fatigue*, 2011, vol. 33, pp. 1417–25.

38. P.S. De and R.S. Mishra: *Sci. Technol. Weld. Join.*, 2011, vol. 16, pp. 343–47.

39. I. Kalemba, S. Dymek, C. Hamilton, and M. Blicharski: *Mater. Sci. Technol.*, 2011, vol. 27, pp. 903–8.

40. A. Denquin, D. Allehaux, G. Lapasset, and H. Ostersehlte: in *Aluminium Alloys: Their Physical and Mechanical Properties, 11th Int. Conf. on Aluminum Alloys*, G. Gottstein, J. Hirsch, B. Skrotzki, eds., John Wiley & Sons, Hoboken, NJ, 2008, pp. 1939–44.

41. V. Barnier, O. Heintz, D.E. Roberts, R. Oltra, and S. Costil: *Surf. Interface Anal.*, 2006, vol. 38, pp. 406–09.

42. K.A.A. Hassan, P.B. Prangnell, A.F. Norman, D.A. Price, and S.W. Williams: *Sci. Technol. Weld. Join.*, 2003, vol. 8, pp. 257–68.

43. S.-W. Song, B.-C. Kim, T.-J. Yoon, N.-K. Kim, I.-B. Kim, and C.-Y. Kang: *Mater. Trans., JIM*, 2010, vol. 51, pp. 1319–25.

44. S.-W. Song, S.-H. Lee, B.-C. Kim, T.-J. Yoon, N.-K. Kim, I.-B. Kim, and C.-Y. Kang: *Mater. Trans., JIM*, 2011, vol. 52, pp. 254–57.

45. D. Steglich, H. Wafai, and W. Brocks: *Int. J. Damage Mech*, 2010, vol. 19, pp. 131–52.

46. D.L. Chen and M.C. Chaturvedi: *Metall. Mater. Trans. A*, 2000, vol. 31A, pp. 1531–41.

47. J.Q. Chen, Y. Madi, T.F. Morgeneyer, and J. Besson: *Comput. Mater. Sci.*, 2011, vol. 50, pp. 1365–71.

48. Y.E. Ma, Z.Q. Zhao, B.Q. Liu, and W.Y. Lia: *Mater. Sci. Eng. A*, 2013, vol. A569, pp. 41–47.

49. W.D. Lockwood, B. Tomaz, and A.P. Reynolds: *Mater. Sci. Eng. A*, 2002, vol. A323, pp. 348–53.

50. H.J. Liu, H. Fujii, M. Maeda, and K. Nogi: *J. Mater. Proc. Technol.*, 2003, vol. 142, pp. 692–96.

51. C. Bitondo, U. Prisco, A. Squillace, G. Giorleo, P. Buonadonna, G. Dionoro, and G. Campanile: *Int. J. Mater. Form.*, 2010, vol. 3, pp. 1079–82.

52. S. Malarvizhi and V. Balasubramanian: *Trans. Nonferrous Met. Soc. China*, 2011, vol. 21, pp. 962–73.

53. C. Gallais, A. Simar, D. Fabrègue, A. Denquin, G. Lapasset, B. de Meester, Y. Bréchet, and T. Pardoen: *Metall. Mater. Trans. A*, 2007, vol. 38A, pp. 964–81.

54. K.L. Nielsen, T. Pardoen, V. Tvergaard, B. de Meester, and A. Simar: *Int. J. Solids Struct.*, 2010, vol. 47, pp. 2359–70.

55. K. Kumar and S.V. Kailas: *Sci. Technol. Weld. Join.*, 2010, vol. 15, pp. 305–11.

56. T. Jene, G. Dobmann, G. Wagner, and D. Eifler: *Proc. 6th International Symposium on Friction Stir Welding*, The Welding Institute, Great Abington, Cambridge, UK, 2006 (paper on CD-ROM).

57. J.E. Barnes, J. Mc Michael, and A. Reynolds: *Proc. 6th International Symposium on Friction Stir Welding*, The Welding Institute, Great Abington, Cambridge, UK, 2006 (paper on CD-ROM).

58. S. Oki, M. Tsujikawa, Y. Okawa, H. Takahara, S.W. Chung, and K. Higashi: *Proc. 6th International Symposium on Friction Stir Welding*, The Welding Institute, Great Abington, Cambridge, UK, 2006 (paper on CD-ROM).

59. W.D. Lockwood and A.P. Reynolds: *Mater. Sci. Eng. A*, 2003, vol. A339, pp. 35–42.

60. C. Genevois, A. Deschamps, and P. Vacher: *Mater. Sci. Eng. A*, 2006, vol. A415, pp. 162–70.

61. J. Besson and R. Foerch: *Comput. Meth. Appl. Mech. Eng*, 1997, vol. 142, pp. 165–87.